Article | Open Access

Energy Materials

Hussain *et al. Energy Mater.* **2026**, *6*, 600151 **DOI:**10.20517/energymater.2026.49

Upcycling waste polyester into cobalt-molybdenum sulfide-decorated carbon foam for photothermal desalination and parametric optimization using Taguchi design of experiments

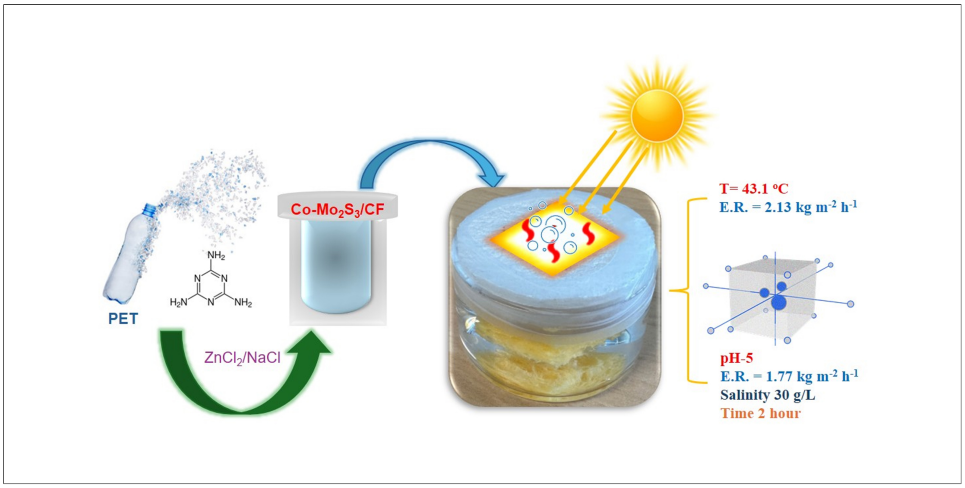
Muzammil Hussain[1,2,3,#], **Ansa Shahzadi**[4,#], **Enrique Rodríguez-Castellón**[5], **Kiran Aftab**[4,*], **Tofik Ahmed Shifa**[1], **Alberto Vomiero**[1,6,*], **Elisa Moretti**[1]

Keywords:
Plastic upcycling, solar evaporators, sulfide nanostructures, photothermal desalination, circular economy

Citation: Hussain, M.; Shahzadi, A.; Rodríguez-Castellón, E.; Aftab, K.; Shifa, T. A.; Vomiero, A.; Moretti, E. Upcycling waste polyester into cobalt-molybdenum sulfide-decorated carbon foam for photothermal desalination and parametric optimization using Taguchi design of experiments. *Energy Mater.* **2026**, *6*, 600151. https://dx.doi.org/10.20517/energymater.2026.49

Received: 31 Mar 2026
First Decision: 12 May 2026
Revised: 4 Aug 2026
Accepted: 21 Sep 2026
Published: 4 Nov 2026

Academic Editor: Xiongwei Wu
Copy Editor: Ping Zhang
Production Editor: Ping Zhang



Abstract

Photothermal desalination is an emerging solar-powered technique for water desalination. One of the primary open issues in the field is the development of new materials that guarantee high photothermal efficiency and evaporation rates. In this study, waste polyethylene terephthalate (PET) bottles are upcycled into carbon foam, which is then decorated with Co-Mo_2S_3 via hydrothermal synthesis to prepare a photothermal evaporator. The as-synthesized Co-Mo_2S_3/carbon foam (CF) achieved an average evaporation rate of 2.13 kg m^{-2} h^{-1} during a 1-h experiment under 1,000 W m^{-2} irradiation using a 3.5% NaCl solution, compared to 1.55 kg m^{-2} h^{-1} obtained for CF. A Taguchi orthogonal-array design of experiments (DOE) was used to optimize the effect of input parameters on the evaporation rate of saline water. The experimental design matrix shows a maximum water evaporation rate of 1.77 kg m^{-2} h^{-1} under real sunlight. Taguchi analysis presents the optimal operating parameters for the evaporation rate as follows: salinity 30 g L^{-1} (level 1), saline water pH 5 (level 2), and time 2 h (level 2). The statistical outcomes show that salinity is the main factor affecting the evaporation rate. This study addresses

[1]Department of Molecular Sciences and Nanosystems, Ca' Foscari University of Venice, Venice 30172, Italy.
[2]Department of Industrial Engineering, University of Padova, Padova 35131, Italy.
[3]Department of Environmental Sciences, Computer Science and Statistics, Ca' Foscari University of Venice, Venice 30172, Italy.
[4]Department of Chemistry, Government College University Faisalabad, Faisalabad 38000, Pakistan.
[5]Department of Inorganic Chemistry, Crystallography and Mineralogy, Faculty of Science, Inter-university Institute of Research in Biorefinery I3B, University of Malaga, Málaga 29071, Spain.
[6]Division of Materials Science, Department of Engineering Sciences and Mathematics, Luleå University of Technology, Luleå 97187,

Sweden.
#Authors contributed equally.

*__Correspondence to:__ Prof. Alberto Vomiero, Division of Materials Science, Department of Engineering Sciences and Mathematics, Luleå University of Technology, Luleå 97187, Sweden. E-mail: alberto.vomiero@ltu.se; Dr. Kiran Aftab, Department of Chemistry, Government College University Faisalabad, Faisalabad 38000, Pakistan. E-mail: drkiranaftab@gcuf.edu.pk

water scarcity and promotes the circular economy by transforming plastic waste into a valuable resource for producing clean water and provides deeper insight into the optimization of the operating parameters using statistical tools.

INTRODUCTION

Modern industrialization and rapid increase in the world population have exacerbated freshwater scarcity, which has become a global issue[1]. Since seawater accounts for 97% of the world's water resources, efforts are underway to desalinate it[2]. Various desalination processes can be implemented, such as reverse osmosis (RO), forward osmosis (FO), membrane distillation (MD), capacitive deionization (CDI), solar still (SS), and humidification-dehumidification desalination (HDH). Interfacial solar steam generation (ISSG) has gained popularity due to its simplicity, the potential use of super-hydrophilic, high-solar-absorbing materials, their self-floating properties, and stability[3-5]. A photothermal material in an interfacial heating system localizes absorbed solar heat at the air-water interface, reducing heat losses and improving steam production efficiency[6,7]. Plastics, particularly polyethylene terephthalate (PET) bottles, have become an integral part of our daily lives, but their widespread use and disposal represent a significant global challenge[8]. Annually, up to 6.3 billion tons of waste plastic have been produced globally, of which 9% has been recycled, 12% incinerated, and 79% accumulated in landfills, as shown in Figure 1[9]. Because waste plastic is not readily biodegradable, it is commonly managed using conventional routes, such as mechanical recycling, incineration, and landfilling, which are regarded as downcycling routes as they reduce its quality[8].

Upcycling of waste polyester, particularly from PET waste bottles, includes transformation of waste items into innovative and higher-value products, which is a sustainable way to reduce "white pollution"[10]. To accomplish a substantial drop in waste production through prevention, recycling, and reuse, the conversion of waste polyester into porous carbons addresses the circular economy aspect that is receiving intense attention from policymakers, companies, and governments[11,12]. Supplementary Table 1 represents the upcycling of waste PET bottles for solar desalination. Utilizing a carbon-based solar evaporator from waste PET bottles may represent a sustainable solution with the capacity to reduce plastic waste and address water scarcity[13-15].

To attain a high solar evaporation rate, four primary subgroups of photothermal materials can be identified, including polymers, inorganic semiconductors, metallic nanostructures, and carbon-based photothermal materials[16-18]. An ideal photothermal material is a substance that absorbs the entire solar spectrum up to 2.5 mm and has a low emissivity at longer wavelengths to avoid blackbody emission. As an innovative photothermal material, carbon foam, whose porous architecture can be readily tailored compared with conventional carbon materials, has attracted increasing interest[19-21]. Furthermore, the combination of a porous hydrophilic carbon foam with properly tuned nanostructures can enhance the evaporation rate during photothermal desalination[22,23].

Hybrid nanocomposites with low thermal conductivity and super-hydrophilic properties are used in a solar steam generation system, enabling optimal broadband absorption, localized heating, reduced heat loss, and enhanced photothermal conversion efficiency. A promising option for light harvesting is the use of

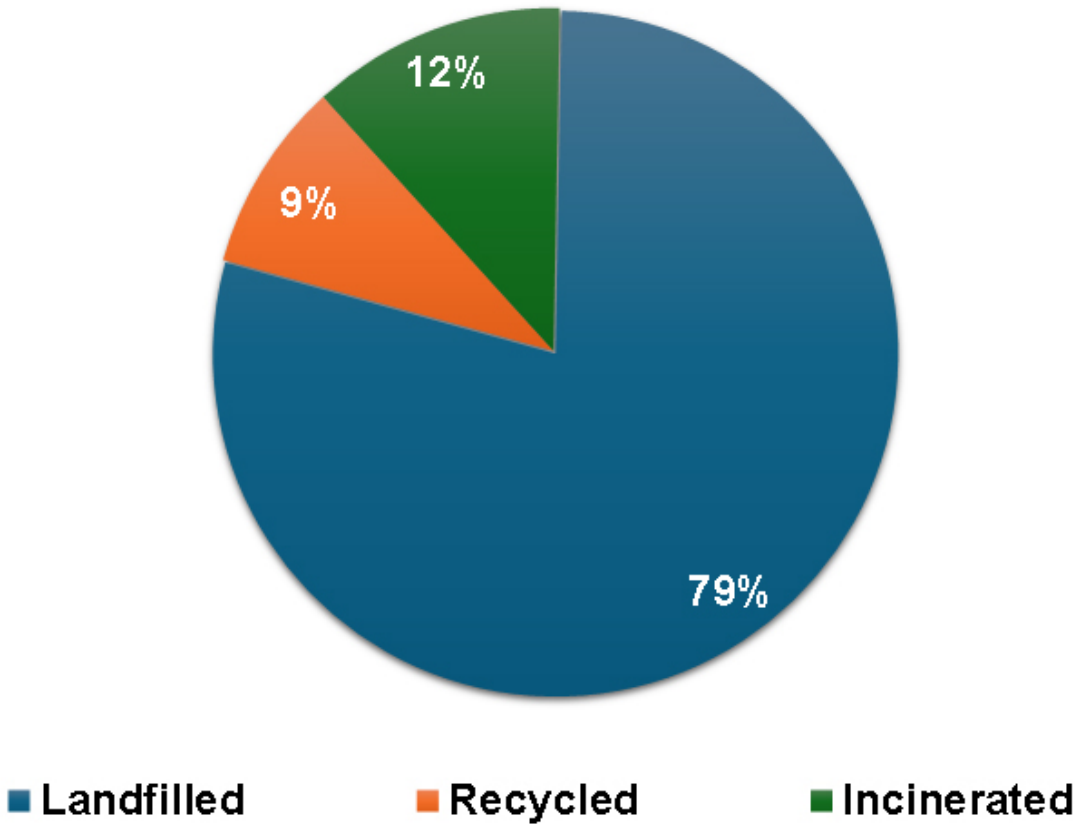


Figure 1. Global plastic waste management statistics.

transition-metal sulfides[24,25]. More than 95% of the entire 290-2,500 nm solar spectrum can be absorbed by photothermal materials composed of sulfide nanostructures having a low band gap (1.3-1.9 eV)[26,27]. Yang *et al.* demonstrated that the hybrid film based on MoS_2 and nanotubes achieved high light-to-heat conversion efficiency[28]. Guo *et al.* conducted structural optimization to increase the evaporation rate of MoS_2-based materials by creating MoS_2-cotton cloth substrates[29], MoS_2-melamine foam[30], 1T/2H phases of MoS_2 nanosheets[31], and MoS_2/C@polyurethane composite sponge[26].

Recent studies have shown that waste PET can be effectively converted into C-based photothermal evaporators for interfacial solar desalination, offering an environmentally sustainable solution for plastic waste valorization. Despite these advances, most plastic waste-derived C-based evaporators rely primarily on the inherent photothermal properties of carbon (e.g., N-doped carbon foam)[32], high-temperature synthesis of graphitic carbon nanosheets at 900 °C from waste plastic mix, and PET-derived MnO/C at 600 °C[33,34], or use only a narrow set of additional photothermal materials such as ZnO porous carbon from waste PET[10], and carbon monoliths derived from PET waste (low evaporation rate 0.99 kg m^{-2} h^{-1} with 63% efficiency)[35]. However, these investigations highlight limitations in developing low-temperature, facile synthesis routes to an efficient solar steam generator from waste plastic. In addition, a systematic understanding of how operating parameters affect desalination performance is lacking, because the aforementioned studies were conducted using one-factor-at-a-time methods rather than statistically designed approaches.

The present study reports a hybrid Co-Mo_2S_3/carbon foam (CF) solar evaporator developed via low-temperature (340 °C) upcycling of PET-derived CF, followed by impregnation with cobalt molybdenum sulfide (Co-Mo_2S_3) using a simple hydrothermal method [Figure 2]. As a result of functionalization with chalcogenides, the Ultraviolet-Visible-Near Infrared (UV/Vis-NIR) absorption is boosted from 68% in NIR

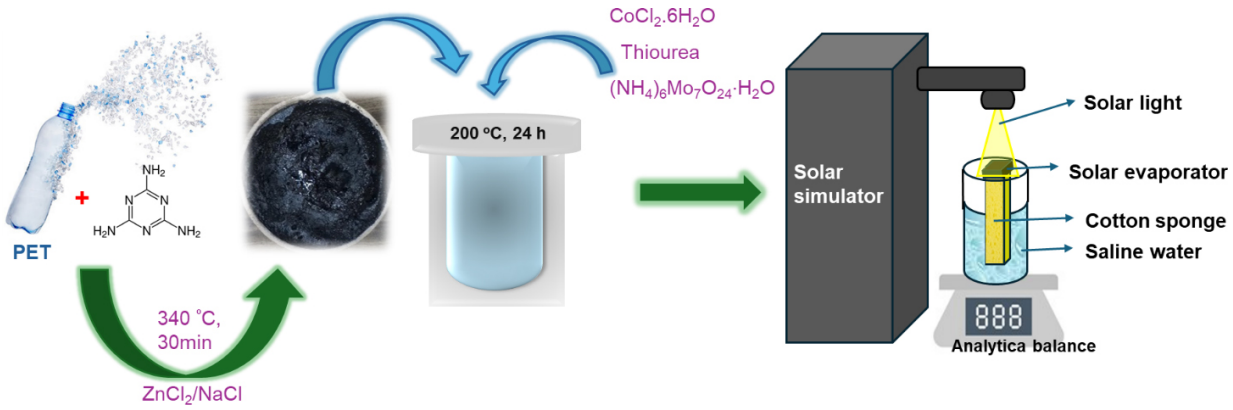


Figure 2. Schematic illustration of Co-Mo_2S_3/CF synthesis and its use in solar desalination. CF: Carbon foam; PET: polyethylene terephthalate.

for CF to 95% for Co-Mo_2S_3/CF. The Co-Mo_2S_3/CF evaporator consequently achieved an evaporation rate of 2.13 kg m^{-2} h^{-1} for Co-Mo_2S_3/CF compared to 1.55 kg m^{-2} h^{-1} for CF. Moreover, Taguchi design of experiments (DOE) was used to optimize and evaluate the effects of several factors (saline water pH, exposure time to sunlight, and salinity) on the evaporation rate, thereby attaining optimal process conditions for solar desalination. Overall, the present work delivers both a PET-derived hybrid photothermal evaporator and a statistically guided process optimization, offering an environmentally friendly approach to address water scarcity and plastic-waste management challenges, thereby enabling circular economy practices.

EXPERIMENTAL

Chemicals and reagents

The solvent, reagents, and chemicals employed in the present research work were bought from Sigma-Aldrich including melamine, $ZnCl_2$, NaCl, $CoCl_2{\cdot}6H_2O$, $(NH_4)_6Mo_7O_{24}{\cdot}H_2O$, thiourea, ethanol, conc. HCl, deionized water, and were used without further purification.

Synthesis of Co-Mo_2S_3/CF

Waste PET bottles were washed with distilled water, air-dried, and then cut into small pieces. Carbon foam was prepared using a mixture of PET (1.5 g), melamine (0.75 g), and eutectic salts ($ZnCl_2$/NaCl, 3 g) at a mass ratio of 58:42, following the method reported by Fechler[36]. It was weighed, mixed uniformly in a crucible, and covered with a lid. The mixture was carbonized for 30 min at 340 °C in a muffle furnace. The heating rate of 10 °C/min was used for the carbonization process. After cooling the muffle furnace to room temperature, the material sample was repeatedly washed with 1 M HCl and deionized water until the filtrate's pH reached neutrality, and dried at 60 °C to obtain CF[22].

CF was impregnated with Co-Mo_2S_3 using a one-step hydrothermal method. 0.124 g $(NH_4)_6Mo_7O_{24}{\cdot}H_2O$ and 0.548 g H_2NCSNH_2 were mixed with 1 g of CF in 15 mL of deionized (DI) water, and stirred for 20 min. Then, 15 mL of an aqueous solution of 1 mmol $CoCl_2{\cdot}$ $6H_2O$ was slowly added to the mixture. The concentrated HCl (300 µL) was added dropwise after mixing the metal salt solutions with CF. Then, the reaction precursor was stirred for a few minutes, and transferred into a Teflon-lined 50 mL stainless steel autoclave. After sealing the autoclave, it was placed in the oven, and the hydrothermal reaction was run for 24 h at 200 °C. After completion of the reaction, the autoclave was cooled to room temperature, the sample was centrifuged at 4,500 rpm, washed repeatedly with ethanol and DI water, and finally dried at 60 °C in a vacuum drying oven[37].

Structural characterization

X-ray diffraction was performed using an Agilent V1000 (USA) diffractometer. X-ray photoelectron spectroscopy (XPS) analysis was performed using a PHI Versa Probe II Scanning XPS Microprobe spectrometer (Physical Electronics PHI, USA) with monochromatic Al Kα radiation as the excitation source (200 μm diameter, 25.0 W, 15 kV, 1,486.6 eV). The peak fitting of the high-resolution spectrum of Mo 3*d* was performed by considering four Mo $3d_{5/2}$-Mo $3d_{3/2}$ doublets with an energy splitting of 3.2 eV and an area ratio of 3:2, using the same Full Width at Half Maximum (FWHM) values for all contributions. The peak fitting of the high-resolution spectrum of S 2*p* was achieved by taking into account three doublets $2p_{3/2}$-S $2p_{1/2}$ with an energy splitting of 1.2 eV, an area ratio 2:1, and using the same FWHM values for all contributions. The spectral analysis was performed using, in most cases, Gaussian-Lorentzian fitting and Shirley background subtraction. UV/Vis-NIR absorption spectra were recorded using a UV/Vis spectrophotometer (LAMBDA 1050+, Perkin Elmer with an integrating sphere). The scanning electron microscopy (SEM) images were acquired using an SEM Cube II (Emcraft, South Korea). Fourier-transform infrared (FTIR) spectra were recorded using a Nicolet 6700 (USA) FTIR spectrometer in transmission mode. Differential scanning calorimetry (DSC) data were acquired using a 1020 Series DSC-7 (USA) thermal analysis system; the temperature range for the experiment was 25 °C to 150 °C under an N_2 atmosphere at a heating rate of 10 °C min^{-1}.

Interfacial solar steam generation

To evaluate the efficiency of the synthesized materials [i.e., cobalt molybdenum sulfide on carbon foam (Co-Mo_2S_3/CF) nanostructures] for solar water desalination, ISSG experiments were conducted. To prepare the solar evaporator, Co-Mo_2S_3/CF (0.1 g in 20 mL deionized water) was initially sonicated for 5 min. Then, Co-Mo_2S_3/CF was deposited on a glass microfiber filter (Whatman GF/F CAT No. 1825-047) through a vacuum filtration system, followed by drying the membrane at 60 °C. A photothermal desalination experiment was performed using 45 mL of salt solution, containing 3.5% NaCl (the average global seawater salinity). The evaporation experiment was carried out under 1,000 W m^{-2} irradiation (air mass 1.5 global, AM1.5G) using a solar simulator (Abet Technologies Model No. 10500, USA), with a 1 cm × 1 cm membrane placed on a hydrophilic carbon sponge. The surface temperature of the solar evaporator under dry and wet conditions was measured using a thermal camera (FLIR C3X, Sweden). Water mass was recorded every 10 min for 1 h and monitored using an analytical balance. The evaporation rate was calculated using[14]:

$$\text{Evaporation rate} = \Delta m / (S \times \tau) \quad (1)$$

where Δm is the mass change of water (kg), S is the evaporation area (m^2), and τ is the evaporation time (h). A similar procedure was used to investigate the evaporation rate under real sunlight.

Furthermore, the evaporation efficiency (η) was estimated using[14]:

$$\eta = \frac{m h_{lv}}{c_{opt} q_i} \quad (2)$$

where h_{lv} is the enthalpy of the evaporated vapor, m is the mass flux (in kg m^{-2} s^{-1}), C_{opt} is the optimal concentration, and q_i is the incident solar radiance (1,000 W m^{-2}).

Taguchi design of experiments

The evaporation rate is affected by both controllable and uncontrollable factors (noise sources). pH of saline water, time of sunlight exposure, and salinity were chosen as the three factors to be investigated[38]. Taguchi orthogonal array DOE was used to optimize the three factors pH (1-9), salinity (30-50 g L^{-1}), and time (1-3 h) at three levels, as shown in Table 1, to evaluate the effect of the operational parameters on the evaporation

Table 1. The studied input process parameters and their respective levels

Sr No.	Parameters	L1	L2	L3
1	pH	1	5	9
2	Time (h)	1	2	3
3	Salinity (g L^{-1})	30	40	50

rate. The experiments were designed using the Minitab Statistical software version 15. An L_9 orthogonal array L_9 (3^4) OA, including three factors at three levels each across nine runs, was utilized, as presented in Supplementary Table 2.

The signal-to-noise ratio (S/N) was determined to measure how much the observed results deviate from the target quality characteristic. The formula used to calculate the larger-the-better (S/N_L) ratio for cases where higher values are preferred is given below[38]:

$$S/N_L = -10 \log_{10} \left[(1/n) \Sigma \left(1/Y_i^2 \right) \right] \quad (3)$$

where n is the number of experiments and Y is the response in each experiment. In these experiments, the system was optimized when the response (evaporation rate) was maximized. The best factor levels are those resulting in the highest S/N_L ratio.

A high S/N ratio signifies that the signal strongly outweighs the effects of noise factors. Processes that achieve the highest S/N ratios tend to deliver superior quality with less variation. In this study, different Taguchi-recommended data analysis techniques have been utilized: (i) constructing average response curves and (ii) conducting analysis of variance (ANOVA) on both raw and S/N ratio data. Graphical representations of the average response curves at each parameter level help visualize trends and show how each parameter affects the outcome.

RESULTS AND DISCUSSION

The X-ray diffraction (XRD) pattern of the Co-Mo_2S_3/CF composite in Figure 3A shows distinct peaks at 17.2°, 25.2°, 28.6°, 32.5°, 47.5°, and 56.4°, which are well indexed as (100), (002), (102), (110), (211) and (212) planes of monoclinic Mo_2S_3 (JCPDS card No. 81-2031)[39]. The broad diffraction feature at approximately 25.2° is attributed to the (002) plane of partly graphitized carbon originating from the carbon-foam substrate. The average crystallite size calculated using Scherrer's equation [Supplementary Equation 1] for the major diffraction peaks (100), (002), (102), (110), (211), and (212) was 13.6 nm. The detailed calculations are presented in Supplementary Section 1.

FTIR was employed to identify the surface functional groups present in the CF. Figure 3B presents the FTIR spectra of the CF and Co-Mo_2S_3/CF. For CF, the main broad band observed near 3,260 cm^{-1} corresponds to OH stretching and NH asymmetric stretching vibrations. Bands detected at 3,063 and 1,740 cm^{-1} are related to the stretching modes of C-H and COOH groups, respectively. The bands at 1,684 and 1,416 cm^{-1} indicate C=N stretching and benzene ring stretching, respectively. The peaks at 1,276 and 1,110 cm^{-1} correspond to the C-O stretching vibration. The FTIR analysis of the synthesized Co-Mo_2S_3/CF showed a band at 3,253 cm^{-1} attributed to the stretching vibration of O-H and the asymmetric N-H vibration. The bands observed at 3,063 cm^{-1} and 1,733 cm^{-1} were assigned to C–H stretching and the C=O stretching vibration of the carboxylic acid (–COOH) group. The sharp bands at 1,682 cm^{-1} and 1,420 cm^{-1} correspond to C=N. The peaks at 1,278 cm^{-1} and 1,110 cm^{-1} correspond to the C-O stretching vibration. For both samples, the peaks at 728 cm^{-1} and 732 cm^{-1} are attributed to Cl_2, which results from washing of CF with HCl. Mo_2S_3 is primarily a metal sulfide;

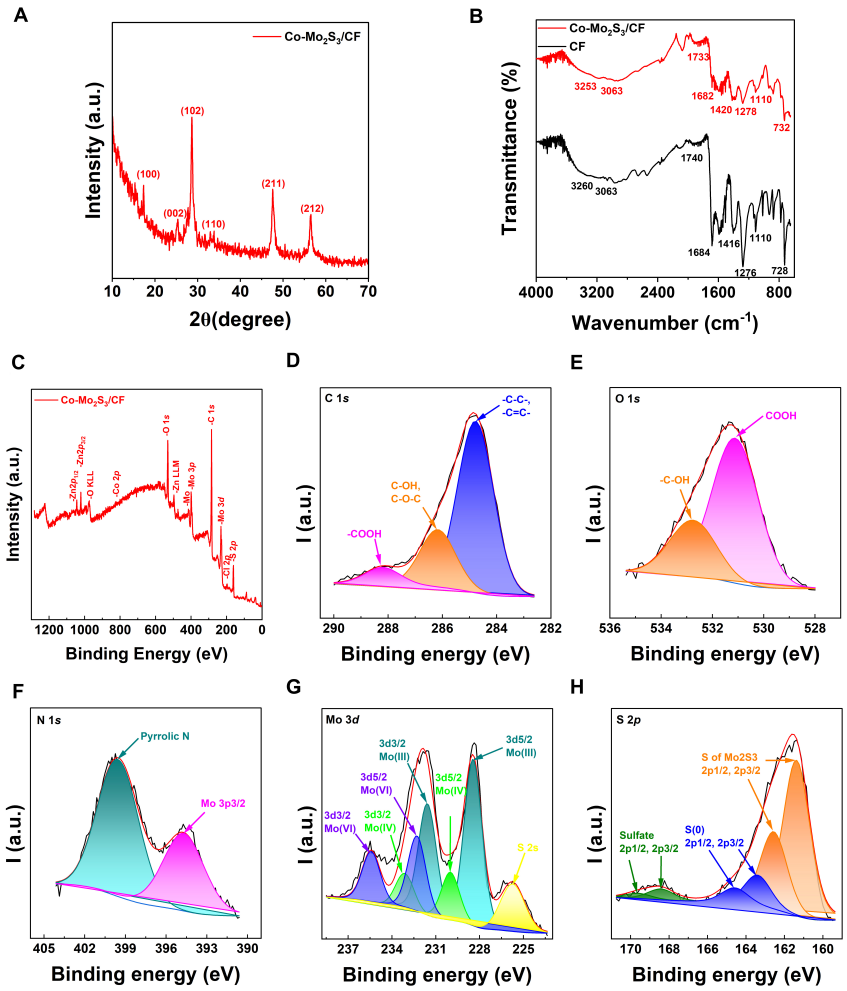


Figure 3. (A) XRD pattern of Co-Mo_2S_3/CF; (B) FTIR spectra of CF and Co-Mo_2S_3/CF; (C) XPS survey spectrum of Co-Mo_2S_3/CF, (D) high-resolution C 1*s*, (E) O 1*s*, (F) N 1*s* and Mo 3*p*, (G) Mo 3*d*, (H) S 2*p*. CF: Carbon foam; XPS: X-ray photoelectron spectroscopy; FTIR: Fourier-transform infrared; XRD: X-ray diffraction.

its vibrations are not always prominent in FTIR due to low infrared activity. FTIR analysis shows that the incorporation of Co-Mo_2S_3 does not alter the surface functionality of CF, which retains all major functional groups of CF. Typical O-H, N-H, C-H, C=O, C=N, and C-O signals remain evident, demonstrating that the carbon-foam structure is preserved during hydrothermal metal sulfide integration.

XPS was used to analyze the surface composition and chemical states of the elements present in the sample. Figure 3C presents the survey spectrum of Co-Mo_2S_3/CF, showing that the sample has elemental concentrations of 72.28%, 15.92%, 2.95%, 6.45%, 0.94%, 0.36, and 1.10% for C, O, Mo, S, Cl, Co, and Zn, respectively. The minor residual Zn and Cl signals appearing in the XPS survey spectrum are attributed to residues linked with the $ZnCl_2$-assisted carbonization process. Figure 3D presents the three contributions for C 1*s* core level at 284.8 eV (-C-C-, -C=C-), 286.2 eV (C-OH, C-O-C), and 288.2 eV (-COOH). Figure 3E presents two O 1*s* contributions at 531.1 and 532.7 eV were assigned to -COOH and -C-OH, respectively. Figure 3F presents the N 1*s* core-level spectrum overlaps with the Mo 3*p* signal. The peak for N 1*s* core level at 399.6 eV corresponds to pyrrolic nitrogen present in the CF structure, and the Mo $3p_{3/2}$ core level is obtained at 394.7 eV. For molybdenum, the Mo 3*d* core-level region shows multiple oxidation states. Figure 3G presents the peaks at 228.4 eV ($3d_{5/2}$) and 231.6 eV ($3d_{3/2}$), which are assigned to Mo(III) species, consistent with Mo_2S_3. Signals at 230.0 eV ($3d_{5/2}$) and 233.1 eV ($3d_{3/2}$) correspond to Mo(IV), typically

observed in MoS_2 or mixed-valence sulfides. Finally, the higher binding-energy doublet at 232.3 eV ($3d_{5/2}$) and 235.4 eV ($3d_{3/2}$) is characteristic of Mo(VI) species, indicating partial oxidation of molybdenum at the surface. The coexistence of Mo(III), Mo(IV), and Mo(VI) suggests a mixed-valence system, likely arising from surface oxidation or local chemical heterogeneity. The Co 2*p* XPS spectrum of the Co-Mo_2S_3/CF sample [Supplementary Figure 1] displays no well-defined peaks. The expected Co $2p_{3/2}$ and Co $2p_{1/2}$ features at approximately 780 eV and 795 eV, typically indicative of Co^{2+} species, are not clearly observed. Instead, the spectrum shows a low-intensity, noisy signal, suggesting that cobalt is either present at very low concentrations or highly dispersed within the Mo_2S_3 matrix [Supplementary Figure 1]. The absence of distinct Co-related peaks indicates that cobalt is incorporated within the host lattice rather than forming segregated cobalt oxide or sulfide phases. The S 2*p* XPS spectrum of Mo_2S_3 [Figure 3H] shows several components corresponding to different sulfur chemical states. The doublet at 161.4 eV (S $2p_{3/2}$) and 162.6 eV (S $2p_{1/2}$) is attributed to sulfur bonded to molybdenum in Mo-S environments characteristic of Mo_2S_3 and MoS_3. Additional peaks at 163.4 eV and 164.6 eV correspond to elemental sulfur (S°) species, while the higher-binding-energy doublet at 168.4 eV and 169.6 eV is assigned to sulfate (SO_4^{2-}) groups. The presence of sulfate peaks suggests partial surface oxidation of the sulfide species.

The SEM images of the synthesized CF and Co-Mo_2S_3/CF composite are shown in Figure 4. The pristine CF exhibits the rough, open-cell porous morphology typical of carbon foams [Figure 4A and B]. After the incorporation of Co-Mo_2S_3, the overall porous framework remains intact; however, the surface becomes rougher due to the uniform deposition of Co-Mo_2S_3 nanoparticles [Figure 4C and D]. The coating of Co-Mo_2S_3, combining large pores from CF with smaller nanoscale Co-Mo_2S_3 features, considerably enhances surface roughness. This morphology indicates that Co-Mo_2S_3 is well distributed across the carbon foam surface, suggesting a favorable photothermal interface for efficient solar-driven desalination compared to bare CF. Furthermore, the elemental composition and distribution of the nanocomposite were examined by Energy-Dispersive X-ray Spectroscopy (EDS). Figure 4E presents the mass sum spectrum of Co-Mo_2S_3/CF and elemental mapping, which clearly indicates the complete elemental composition of the nanocomposite, including the incorporation of cobalt.

The absorption spectra of the investigated samples were measured with a UV/Vis spectrophotometer. Figure 5A presents the UV/Vis-NIR spectra of CF and Co-Mo_2S_3/CF. The optical spectra show that Co-Mo_2S_3/CF exhibits absorption greater than 95% throughout the UV/Vis-NIR spectral region, compared with CF, whose absorption decreases from 91% to 68% in the NIR region. The higher light absorption of Co-Mo_2S_3/CF is most likely due to the contribution of sulfide nanostructures. Based on the enhanced absorption, higher photothermal steam generation is expected from the synthesized nanocomposite.

To evaluate the evaporation efficiency of Co-Mo_2S_3/CF, an ISSG experiment using the Co-Mo_2S_3/CF solar evaporator was conducted under simulated solar light (1,000 W m^{-2}). The interfacial solar desalination experiment was repeated three times to calculate the mean values of the change in mass. The evaporation rate for Co-Mo_2S_3/CF and CF, with error bars, is presented in Figure 5B and C. The Co-Mo_2S_3/CF sample achieved an average evaporation rate of 2.13 kg m^{-2} h^{-1} during the one-hour experiment, compared to 1.55 kg m^{-2} h^{-1} achieved by CF [Figure 5B and C]. The continuous decrease in mass indicates that Co-Mo_2S_3/CF enhances photothermal steam generation. In-field tests under direct sunlight indicate an evaporation rate of 1.77 kg m^{-2} h^{-1} for Co-Mo_2S_3/CF. The experiment was conducted on 23 July 2024 under the following weather conditions: relative humidity ≈ 49% and temperature = 39 °C at Government College University Faisalabad, Pakistan. Thermal images of the membrane were recorded using a thermal camera (FLIR C3-X). The CF and Co-Mo_2S_3/CF were found to have dry surface temperatures of 66 °C and 83 °C, respectively, as shown in Figure 5D. The wet surface temperature was 34.6 °C for CF and 43.1 °C for Co-Mo_2S_3/CF. The enhanced surface temperature highlights the role of Co-Mo_2S_3 functionalization on CF.

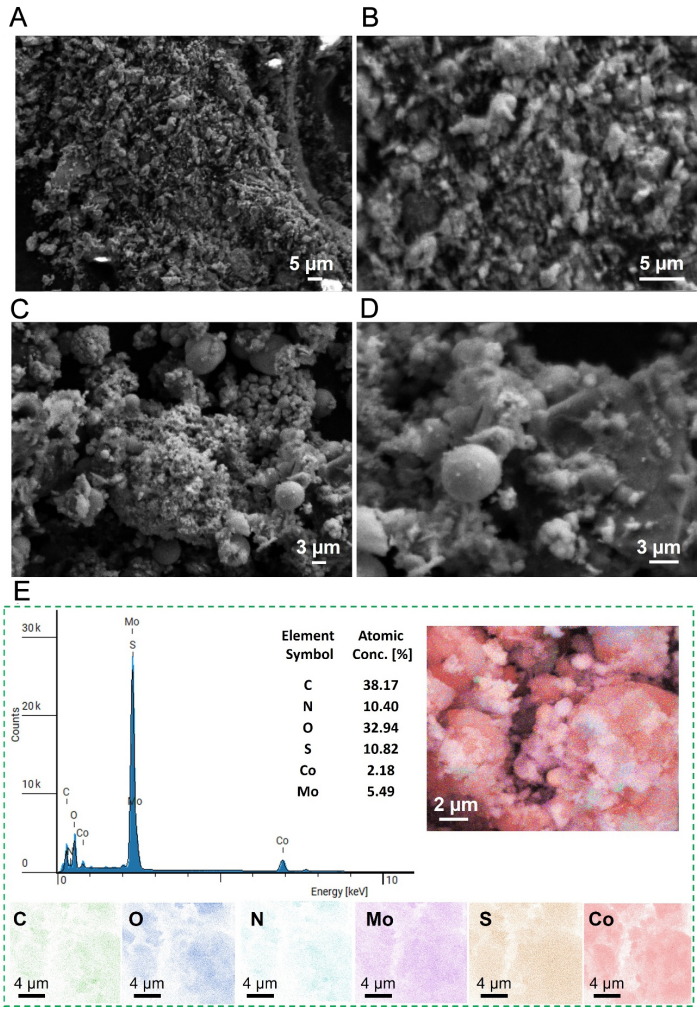


Figure 4. SEM images of CF (A and B), Co-Mo_2S_3/CF (C and D), and (E) EDS mass sum spectrum and elemental mapping of Co-Mo_2S_3/CF. Individual elemental maps were acquired from a selected region of the multielement map. CF: Carbon foam; SEM: scanning electron microscopy; EDS: energy-dispersive X-ray spectroscopy.

Co-Mo_2S_3/CF exhibited relatively high photothermal conversion compared with CF, which ultimately results in an enhanced evaporation rate. Material hydrophilicity is a key factor for efficient solar desalination. Faster water transport can promote a higher solar steam generation rate. To investigate the hydrophilicity of CF and Co-Mo_2S_3/CF, contact angle measurements were performed. Figure 5E shows that CF is hydrophilic. Co-Mo_2S_3/CF is also hydrophilic, although the residence time of the droplet is significantly longer than that on CF.

The evaporation efficiency of the best-performing Co-Mo_2S_3/CF sample was evaluated using the water vaporization enthalpy derived from DSC analysis (see Supplementary Figure 2A). The solar evaporator Co-Mo_2S_3/CF exhibited an excellent evaporation efficiency of 91%. The Co-Mo_2S_3/CF demonstrates its potential as a high-performance solar steam generator. The evaporation rate is a crucial factor in assessing the effectiveness of solar evaporators. In this context, the stability test assesses whether the evaporation rate remains consistent, predictable, and reliable over time. In highly saline aqueous environments, monitoring the evaporation rate over an extended period of time reveals how gradual salt accumulation impacts the

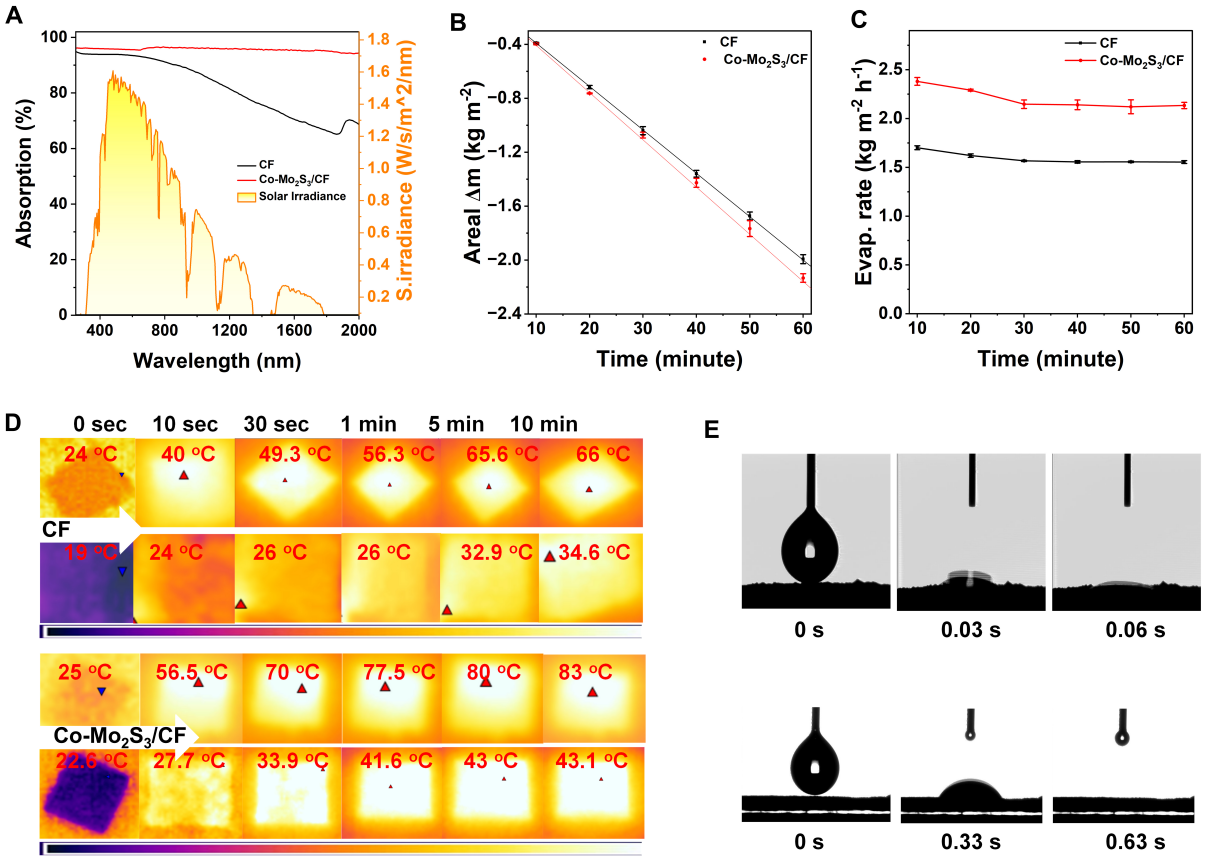


Figure 5. (A) UV/Vis-NIR absorption spectra; (B and C) Areal change in mass and evaporation rate with mean error bars; (D) Dry (upper row) and wet (lower row) surface temperatures, and (E) Contact angle images of CF and Co-Mo_2S_3/CF samples. CF: Carbon foam; UV/Vis-NIR: ultraviolet-visible-near infrared.

evaporation rate. In addition to improving efficiency, operational stability has emerged as a key area of research, prompting the creation of evaporators with integrated salt-resistant features[40].

To assess the performance of Co-Mo_2S_3/CF over a longer duration, the interfacial solar desalination test was performed using a 2.5 × 2.5 cm^2 solar evaporator under 1,000 W m^{-2} irradiance. The solar steam generator was placed on a microfiber membrane, which was insulated with thermal-insulating material and Parafilm to avoid extra evaporation and to maximize the localized heat at the surface of the evaporator (see Figure 6A). The saline water concentration was kept the same as for the earlier experiment (3.5% salinity). The stability test was performed continuously for 6 h under one-sun solar irradiance. The results show that Co-Mo_2S_3/CF maintained an evaporation rate of 2.18 kg m^{-2} h^{-1} on day 1 for 6 h under continuous operating conditions (see Figure 6B). Figure 6C presents the temperature and humidity during the 6 h of the experiment. To investigate the reproducibility, salt accumulation, and self-cleaning of the Co-Mo_2S_3/CF, a stability test was performed over three cycles (each cycle lasted 6 h). During the second and third stability cycles, the solar steam generator was placed on a carbon sponge immersed in deionized water to facilitate self-cleaning of the evaporator. The evaporation rate of 2.16 kg m^{-2} h^{-1} after the third cycle proves the excellent performance of the Co-Mo_2S_3/CF as a solar steam generator. The mean evaporation rate (errors bar) over the 6 h of each cycle is presented as a line graph in Figure 6B. To evaluate the self-cleaning behavior of Co-Mo_2S_3/CF as a solar evaporator, EDS analysis was conducted after the 3rd cycle of the stability test, the evaporator was then placed on a microfiber membrane soaked in distilled water to assess salt (NaCl) removal. Supplementary Figure 2B and C presents the EDS mass-sum spectra of the solar evaporator before and after self-cleaning, and the results clearly demonstrate excellent salt dissolution, with a reduction in Na atomic concentration

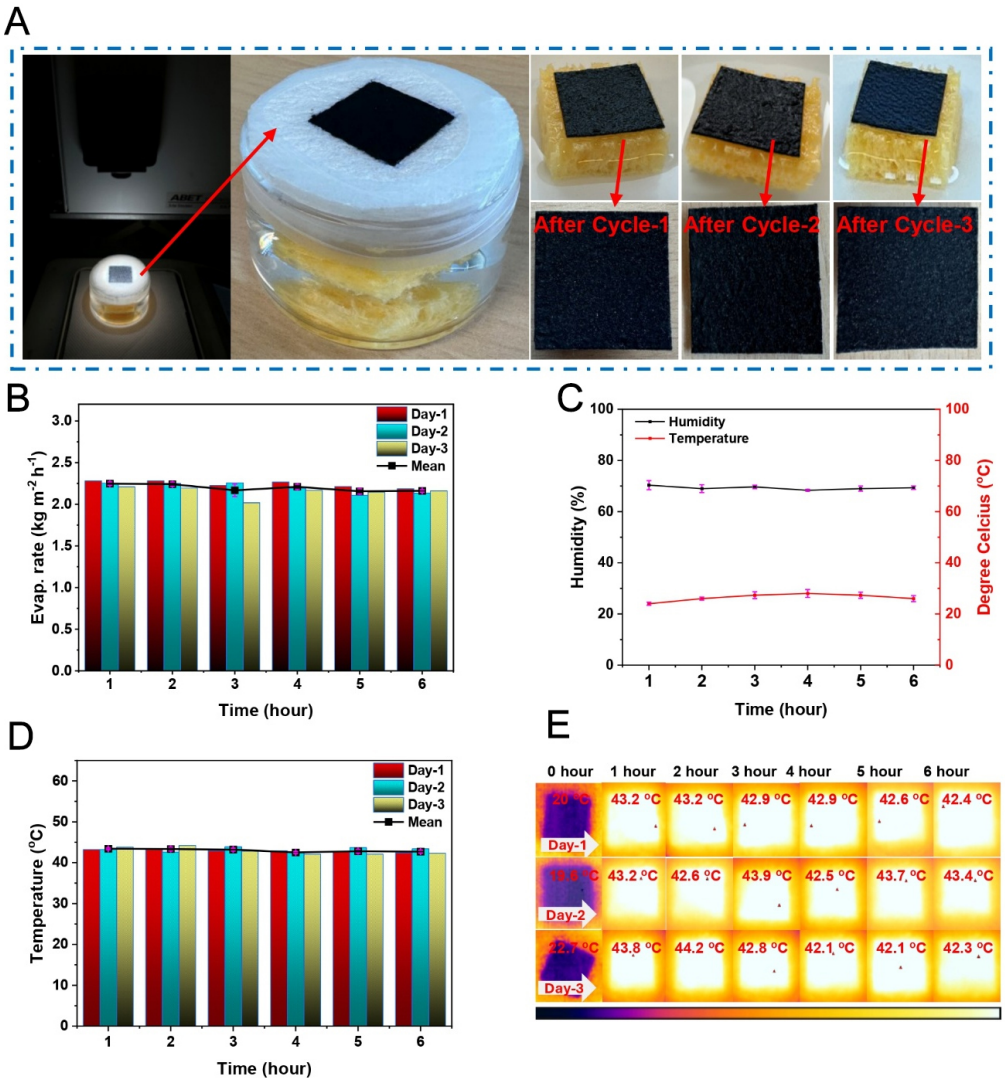


Figure 6. (A) Device configuration and self-cleaning process of the solar evaporator, (B) Evaporation rate during stability testing for each cycle shown as a bar graph at hourly intervals and the line plot with markers represents the mean evaporation rate at each hourly interval, (C) Humidity and room temperature during the stability test, (D) Wet surface temperature of each cycle as a bar graph with hourly intervals and the line plot with marker shows the mean value at each hour interval, (E) Wet surface thermal images during stability test for each cycle of Co-Mo_2S_3/CF. CF: Carbon foam.

from 6.51% to 0.32%. The self-cleaning property of the solar evaporator guarantees stable behavior, resulting in a repeatable evaporation rate of Co-Mo_2S_3/CF. The surface temperature of the solar evaporator plays a substantial role in maintaining the evaporation rate over an extended period. Likewise, for each cycle, the surface temperature of Co-Mo_2S_3/CF during the stability test was recorded with a thermal camera [Figure 6D and E]. The results clearly demonstrate that the Co-Mo_2S_3/CF sample maintains a wet surface temperature of 42.2 °C during each 6-h operating cycle, indicating good thermal stability and repeatable photothermal performance.

The Taguchi orthogonal array DOE enabled researchers to optimize three factors at three levels, to analyze the effects of operational parameters on the water evaporation rate and determine optimal process conditions for solar desalination. An S/N_L type of performance characteristic was used to identify the optimal evaporation rate. Table 2 provides information on the experimental design matrix with process parameters and their levels. As shown, the levels of factors are as follows: pH (1, 5, and 9); Time (1, 2, and 3 h); Salinity

Table 2. Experimental design matrix with response for desalination using Co-Mo_2S_3/CF

Factors				Response	
Exp. Run	**pH**	**Time (h)**	**Salinity (g L^{-1})**	**Mean evaporation rate (kg m^{-2} h^{-1})**	**S/N**
1	1	1	30	1.65	4.35
2	1	2	40	1.71	4.66
3	1	3	50	1.68	4.51
4	5	1	40	1.66	4.40
5	5	2	50	1.68	4.53
6	5	3	30	1.77	4.96
7	9	1	50	1.72	4.71
8	9	2	30	1.72	4.74
9	9	3	40	1.66	4.42

CF: Carbon foam.

(30, 40, and 50 g L^{-1}). The nine experiments were designed [Supplementary Table 2]. To estimate experimental variability, each experiment was repeated three times. The mean evaporation-rate response and signal-to-noise ratio for each experimental run were calculated [Table 2]. The results revealed that the mean evaporation rate ranged from 1.65 to 1.77 kg m^{-2} h^{-1}, and the S/N ratio ranged from 4.35 to 4.96, depending on the specific combination. As Table 2 shows, the maximum evaporation rate of 1.77 kg m^{-2} h^{-1} was obtained with experimental run 6 at pH 5, 3 h of sunlight exposure, and a salinity of 30 g L^{-1}. Analysis of variance was conducted to determine the parameters and their confidence levels for achieving the maximum evaporation rate. An ANOVA was carried out to test whether the process parameters were significant. To identify influential process parameters, the basic *F*-test was used to determine which process parameter significantly influences the evaporation rate. For each parameter, the *F* value was calculated as the ratio of the mean square to the mean square error. In general, a higher *F* value indicates a greater influence on attaining the maximum evaporation rate. ANOVA and performance analysis reveal the best combination of all the process parameters.

Supplementary Figure 3 illustrates the effect of each factor on the S/N_L ratio and mean water evaporation rate. When evaluating the influence of process parameters, salinity had the greatest effect on the overall desalination process using Co-Mo_2S_3/CF, followed by time and then pH. Thus, the Taguchi analysis enables optimization of the input parameters to maximize output. In Table 3, the Taguchi analysis estimates the main effect of each parameter by averaging the evaporation rate associated with each level. The average evaporation rate in Table 3 is calculated from the values in Table 2 by grouping the experimental run data for each factor (pH, time, salinity) and its corresponding level (1, 2, 3) to identify the optimal parameter settings. Based on the Taguchi experimental design, Co-Mo_2S_3/CF showed favorable performance at the slightly acidic pH of 5 (level 2), as shown in Supplementary Figure 4. The results indicated that evaporation rates declined slightly when the pH was decreased to 1. The highest evaporation rate occurred after 2 h of sunlight exposure at level 2, as shown in Supplementary Figure 4. Analysis of the Taguchi orthogonal array further revealed that a 30 g L^{-1} saline solution yielded the maximum evaporation rate with Co-Mo_2S_3/CF (see Supplementary Figure 4). In Ref.[38], the authors found a similar trend in their study on the effect of salinity on the evaporation rate of saline water, conducted at NaCl concentrations of 50, 100, and 150 g L^{-1}. According to Table 2, the experimental run six showed the highest evaporation rate at pH 5, 3 h, and 30 g L^{-1}, but according to Table 3, the calculated values for evaporation rate and S/N_L at 2 h and 3 h are similar. So, these observations indicate that time has no significant effect, and statistical analysis suggests 2 h as the optimal time. Therefore, the optimal operating parameters for evaporation rate are as follows: salinity 30 g L^{-1} (level 1), saline water pH 5 (level 2), and time 2 h (level 2), as shown in Table 3. According to

Table 3. Mean evaporation rate and S/N_L ratio at each factor level obtained from the Taguchi method

Parameter	Level	Average evaporation rate (kg m^{-2} h^{-1})	S/N_L	Rank
pH	1	1.68	4.50	2
	5	1.70	4.63	
	9	1.70	4.62	
Time (h)	1	1.67	4.51	3
	2	1.70	4.61	
	3	1.70	4.61	
Salinity (g L^{-1})	30	1.71	4.66	1
	40	1.67	4.45	
	50	1.69	4.56	

Supplementary Figures 3 and 4, increasing the pH and sunlight exposure time while decreasing the salinity results in a rise in the mean responses of the evaporation rate and S/N_L.

To maximize both the mean response and the S/N_L, the optimal operating conditions were identified as pH 5, time 2 h, and salinity 30 g L^{-1}. The results of the analysis of variance of the obtained data and the *F*-test indicated that the process parameters were not statistically significant ($P > 0.05$), showing that their effects on the evaporation rate were not statistically significant under the tested conditions. Additional variables that may affect solar evaporation require further investigation. Among the tested factors, salinity showed the largest effect on the evaporation rate. To further elaborate on the salinity effect, the solar desalination experiments were performed at different salt concentrations (3.5%, 7%, 10%, and 20%) [Supplementary Figure 5]. The evaporation rate remained steady at moderate salinity when the NaCl concentration ranged from 3.5 to 7 wt%, but a further increase in salt concentration caused a sharp drop in evaporation rate from 2.13 kg m^{-2} h^{-1} at 3.5% to 1.20 kg m^{-2} h^{-1} at 20 wt% NaCl. Increasing salt concentration decreases water vapor pressure due to reduced water activity, thereby lowering the thermodynamic driving force for evaporation. In addition, Na^+ and Cl^- ions form hydration shells with surrounding water molecules, increasing the energy required for water molecules to escape into the vapor phase. Furthermore, the increase in salinity reduced the capillary transport of bulk water through the substrate towards the evaporation interface. This pronounced reduction in evaporation rate cannot be explained by vapor pressure lowering alone. Rather, it reflects the combined effects of reduced water activity, increased solution viscosity, and the onset of local salt accumulation at the evaporation interface. A mechanically robust evaporator is essential for solar steam generators, as continuous exposure to water flow, salt crystallization, thermal cycling, and mechanical handling can compromise their assembly and decrease the evaporation efficiency. An evaporator with mechanical robustness preserves its structural integrity and performance during prolonged use, making it more suitable for real-world water desalination and purification. Enhancing mechanical durability is crucial for ensuring the long-term reliability and scalability of solar evaporators[41-43]. Overall, the current outcomes indicate that future progress in interfacial solar desalination should extend beyond developing new materials and also address factors that limit photothermal conversion efficiency and evaporation rate. As high-performance photothermal evaporators approach their maximum potential under typical operating conditions, it becomes increasingly important to address challenges such as mass-transport limitations, salt accumulation, and the need for effective operation in hypersaline environments. Combining advanced photothermal materials engineering with statistically based process optimization (with expanded operational ranges for improved experimental control) provides a promising route to developing robust, scalable, and energy-efficient solar desalination technologies capable of treating water with rising salinity levels.

CONCLUSIONS

This study utilized waste PET bottles to synthesize CF materials. Further, the deposition of a photothermally

active layer composed of nanostructured Co-Mo_2S_3 enhanced interfacial solar desalination performance through broadened solar light absorption in the NIR spectral region. The as-synthesized material was characterized by XRD and SEM, together with UV/Vis and FTIR spectroscopy. The structure of the CF, together with the increase in the optical absorbance of the Co-Mo_2S_3, resulted in an average evaporation rate of 2.13 kg m^{-2} h^{-1} during a 1-h experiment, as compared to the bare CF (1.55 kg m^{-2} h^{-1}) under 1000 W m^{-2} irradiation using a 3.5% NaCl solution. A Taguchi DOE was used to identify the optimal settings for three variables: exposure time (2 h), pH (5), and salinity (30 g L^{-1}) to achieve an optimal evaporation rate under natural sunlight. The results show that increasing the duration of sunlight exposure and decreasing salinity improve the evaporation rate of saline water. The ANOVA results show that these operating parameters were not statistically significant. So, future research should focus on standardized testing and reporting processes to optimize these parameters. These results provide a sound basis for further development in photothermal material synthesis to unlock even higher efficiencies in the solar-driven clean water generation process, and for statistically guided optimization of operating parameters.

DECLARATIONS

Authors' contributions

Supervised the research and revised the manuscript: Vomiero, A.; Aftab, K.
Performed the materials synthesis, conducted the Taguchi design-of-experiments analysis (DOE), and incorporated the relevant section into the manuscript: Shahzadi, A.
Performed the solar desalination experiments, data analysis and interpretation, manuscript drafting, and revision: Hussain, M.
Revised the paper and provided useful insights for the correct presentation of the data: Moretti, E.
Provided access to the XPS facility: Rodríguez-Castellón, E.
Performed EDS analysis: Shifa, T. A.

Availability of data and materials

The original contributions presented in this study are included in the article/Supplementary Materials. Further inquiries can be directed to the corresponding authors.

AI and AI-assisted tools statement

Not applicable.

Financial support and sponsorship

This work was financially supported by Fundación Bancaria UNICAJA and the Erasmus+ programme through H2EXCELLENCE, as well as by the Spanish Ministry of Science and Innovation (MSI/MCIN) under Grant No. PID2025-171274OB-C22, funded by MCIN/AEI/10.13039/501100011033 and FEDER funds.

Conflicts of interest

All authors declared that there are no conflicts of interest.

Ethical approval and consent to participate

Not applicable.

Consent for publication

Not applicable.

Copyright

© The Author(s) 2026.

Supplementary Materials

Supplementary Materials

REFERENCES

1. Chen, B.; Liu, L.; Song, Y.; et al. Functional upcycling of waste polyester into Cr-MOF towards synergistic interfacial solar evaporation and organic pollutant degradation. *Mater. Today. Sustain.* **2023**, *24*, 100561. DOI
2. Liu, N.; Hao, L.; Zhang, B.; Niu, R.; Gong, J.; Tang, T. Rational design of high-performance bilayer solar evaporator by using waste polyester-derived porous carbon-coated wood. *Energy. Environ. Mater.* **2022**, *5*, 617-26. DOI
3. Chen, C.; Kuang, Y.; Hu, L. Challenges and opportunities for solar evaporation. *Joule* **2019**, *3*, 683-718. DOI
4. Karami, S.; Roghabadi, F. A.; Maleki, M.; Ahmadi, V.; Sadrameli, S. M. Materials and structures engineering of sun-light absorbers for efficient direct solar steam generation. *Solar. Energy.* **2021**, *225*, 747-72. DOI
5. Ahmad, M. M.; Ma, Y.; Saravanan, V.; et al. Facile construction of a super hydrophilic and highly porous $Ti_3C_2T_x$/alginate aerogel solar evaporator for water evaporation and purification. *Sep. Purif. Technol.* **2025**, *371*, 133363. DOI
6. Chen, B.; Ren, J.; Song, Y.; et al. Upcycling waste poly(ethylene terephthalate) into a porous carbon cuboid through a MOF-derived carbonization strategy for interfacial solar-driven water-thermoelectricity cogeneration. *ACS. Sustainable. Chem. Eng.* **2022**, *10*, 16427-39. DOI
7. Ahmad, M. M.; Fatima, A.; Ma, Y.; et al. A robust $Ti_3C_2T_x$/alginate hydrogel reinforced with wheat straw cellulose microfibers (CMFs) for highly durable solar-driven water evaporation and desalination. *Sustain. Mater. Technol.* **2026**, *47*, e01924. DOI
8. Yang, J.; Li, Z.; Xu, Q.; et al. Towards carbon neutrality: sustainable recycling and upcycling strategies and mechanisms for polyethylene terephthalate via biotic/abiotic pathways. *Eco. Environ. Health.* **2024**, *3*, 117-30. DOI PubMed PMC
9. Geyer, R.; Jambeck, J. R.; Law, K. L. Production, use, and fate of all plastics ever made. *Sci. Adv.* **2017**, *3*, e1700782. DOI PubMed PMC
10. Hao, L.; Liu, N.; Zhang, B.; Niu, R.; Gong, J.; Tang, T. Waste-to-wealth: Sustainable conversion of polyester waste into porous carbons as efficient solar steam generators. *J. Taiwan. Inst. Chem. Eng.* **2020**, *115*, 71-8. DOI
11. Elia, V.; Gnoni, M. G.; Tornese, F. Measuring circular economy strategies through index methods: a critical analysis. *J. Clean. Prod.* **2017**, *142*, 2741-51. DOI
12. Lu, Y.; Dong, J.; Guo, G.; et al. Sustainable conversion of waste polyester fibers into high-performance porous carbon for CO_2 capture. *Ind. Eng. Chem. Res.* **2025**, *64*, 15034-44. DOI
13. Hussain, M.; Ibrahim, K. B.; Rodríguez-Castellón, E.; et al. Upcycled PET-derived carbon foam functionalized with Cu_3SbS_4-Sb_2S_3 heterostructures for efficient interfacial solar desalination. *Small* **2025**, *21*, e06862. DOI
14. Hussain, M.; Taranova, A.; Ibrahim, K. B.; et al. Decoration of two-dimensional Cus nanoflakes on graphitic carbon foam derived from waste plastic for interfacial solar desalination. *Solar. RRL.* **2025**, *9*, 2400777. DOI
15. Bai, H.; He, P.; Hao, L.; et al. Engineering self-floating Fe_2O_3/N,O-doped carbon foam as a bifunctional interfacial solar evaporator for synergetic freshwater production and advanced oxidation process. *J. Environ. Chem. Eng.* **2022**, *10*, 108338. DOI
16. Gan, Z.; Sun, W.; Zhao, S.; et al. Hierarchical porous structure salt-resistance carbon-based aerogel for efficient solar-driven interfacial steam generation. *Chem. Eng. J.* **2024**, *495*, 153694. DOI
17. Yu, B.; Zhang, Y.; Wang, Y.; Zhang, Z. Recent advances and challenges of metal-based materials for solar steam generation. *Adv. Funct. Mater.* **2023**, *33*, 2307533. DOI
18. Zhu, M.; Zhang, R.; Yuan, S.; Liu, P. Advances in cellulose materials for interfacial water evaporation and their applications in seawater desalination. *Desalination* **2025**, *601*, 118559. DOI
19. Wang, X.; Liu, Q.; Wu, S.; Xu, B.; Xu, H. Multilayer polypyrrole nanosheets with self-organized surface structures for flexible and efficient solar-thermal energy conversion. *Adv. Mater.* **2019**, *31*, e1807716. DOI
20. Xu, W.; Xing, Y.; Liu, J.; et al. Efficient water transport and solar steam generation via radially, hierarchically structured aerogels. *ACS. Nano.* **2019**, *13*, 7930-8. DOI
21. Zhang, L.; Tang, B.; Wu, J.; Li, R.; Wang, P. Hydrophobic light-to-heat conversion membranes with self-healing ability for interfacial solar heating. *Adv. Mater.* **2015**, *27*, 4889-94. DOI
22. Bai, H.; Liu, N.; Hao, L.; et al. Self-floating efficient solar steam generators constructed using super-hydrophilic N,O dual-doped carbon foams from waste polyester. *Energy. Environ. Mater.* **2022**, *5*, 1204-13. DOI
23. Hussain, M.; Shifa, T. A.; Shinde, P. V.; et al. Enhanced solar water desalination by $CuCo_2S_4$-decorated carbon foam derived from waste plastics. *Chem. Res. Chin. Univ.* **2024**, *40*, 548-55. DOI
24. Chen, R.; Wang, X.; Gan, Q.; Zhang, T.; Zhu, K.; Ye, M. A bifunctional MoS_2 -based solar evaporator for both efficient water evaporation and clean freshwater collection. *J. Mater. Chem. A.* **2019**, *7*, 11177-85. DOI
25. Zhu, Q.; Xu, Q.; Du, M.; et al. Recent progress of metal sulfide photocatalysts for solar energy conversion. *Adv. Mater.* **2022**, *34*, e2202929. DOI

26. Li, W.; Tekell, M. C.; Huang, Y.; Bertelsmann, K.; Lau, M.; Fan, D. Synergistic high-rate solar steaming and mercury removal with MoS_2/C@ polyurethane composite sponges. *Adv. Energy. Mater.* **2018**, *8*, 1802108. DOI
27. Wang, Z.; Yu, K.; Gong, S.; Mao, H.; Huang, R.; Zhu, Z. Cu_3BiS_3/MXenes with excellent solar-thermal conversion for continuous and efficient seawater desalination. *ACS. Appl. Mater. Interfaces.* **2021**, *13*, 16246-58. DOI
28. Yang, X.; Yang, Y.; Fu, L.; et al. An ultrathin flexible 2D membrane based on single-walled nanotube-MoS_2 hybrid film for high-performance solar steam generation. *Adv. Funct. Mater.* **2018**, *28*, 1704505. DOI
29. Guo, Z.; Wang, G.; Ming, X.; et al. PEGylated self-growth MoS_2 on a cotton cloth substrate for high-efficiency solar energy utilization. *ACS. Appl. Mater. Interfaces.* **2018**, *10*, 24583-9. DOI
30. Zhang, W.; Zhu, W.; Shi, S.; Hu, N.; Suo, Y.; Wang, J. Bioinspired foam with large 3D macropores for efficient solar steam generation. *J. Mater. Chem. A.* **2018**, *6*, 16220-7. DOI
31. Ghim, D.; Jiang, Q.; Cao, S.; Singamaneni, S.; Jun, Y. Mechanically interlocked 1T/2H phases of MoS_2 nanosheets for solar thermal water purification. *Nano. Energy.* **2018**, *53*, 949-57. DOI
32. Song, C.; Zhang, B.; Hao, L.; et al. Converting poly(ethylene terephthalate) waste into N-doped porous carbon as CO_2 adsorbent and solar steam generator. *Green. Energy. Environ.* **2022**, *7*, 411-22. DOI
33. Aizudin, M.; Goei, R.; Ong, A. J.; et al. Sustainable development of graphitic carbon nanosheets from plastic wastes with efficient photothermal energy conversion for enhanced solar evaporation. *J. Mater. Chem. A.* **2022**, *10*, 19612-7. DOI
34. Fan, Z.; Ren, J.; Bai, H.; et al. Shape-controlled fabrication of MnO/C hybrid nanoparticle from waste polyester for solar evaporation and thermoelectricity generation. *Chem. Eng. J.* **2023**, *451*, 138534. DOI
35. Alfaro-barajas, A.; Vega-hincapié, D. J.; Hdz-garcia, H.; Oliva, J.; Herrera-trejo, M.; Mtz-enriquez, A. I. Carbon monoliths from PET wastes for interfacial solar evaporation. *Mater. Lett.* **2021**, *294*, 129796. DOI
36. Fechler, N.; Fellinger, T. P.; Antonietti, M. "Salt templating": a simple and sustainable pathway toward highly porous functional carbons from ionic liquids. *Adv. Mater.* **2013**, *25*, 75-9. DOI PubMed
37. Guo, Z.; Yu, F.; Chen, Z.; Shi, Z.; Wang, J.; Wang, X. Stabilized Mo_2S_3 by FeS_2 based porous solar evaporation systems for highly efficient clean freshwater collection. *Sol. Energy. Mater. Sol. Cells.* **2020**, *211*, 110531. DOI
38. Mohammadi, T.; Safavi, M. A. Application of Taguchi method in optimization of desalination by vacuum membrane distillation. *Desalination* **2009**, *249*, 83-9. DOI
39. Chaubey, P.; Sarkar, S.; Sharma, P. K. A multi-interface SnO_2-Co_3O_4-Mo_2S_3 nanocomposite for enhanced electrocatalytic water splitting. *Surf. Interfaces.* **2025**, *72*, 107099. DOI
40. Wu, J.; Liu, J.; Yin, G.; et al. Interfacial solar steam generation at the water-energy nexus: Materials, mechanisms, and multifunctional integration. *Mater. Sci. Eng. R. Rep.* **2026**, *169*, 101209. DOI
41. Guo, S.; Patel, S.; Wang, J.; et al. Self-powered green energy-harvesting and sensing interfaces based on hygroscopic gel and water-locking effects. *Sci. Adv.* **2025**, *11*, eadw5991. DOI
42. Zhang, L.; Zhang, Y.; Li, X.; et al. Moiré superlattice-driven bionic hydrogel robot with programmable multifunctionality. *Nat. Commun.* **2026**, 17. DOI PubMed PMC
43. Zhao, F.; Zhou, X.; Shi, Y.; et al. Highly efficient solar vapour generation via hierarchically nanostructured gels. *Nat. Nanotechnol.* **2018**, *13*, 489-95. DOI

Disclaimer/Publisher's Note: All statements, opinions, and data contained in this publication are solely those of the individual author(s) and contributor(s) and do not necessarily reflect those of OAE and/or the editor(s). OAE and/or the editor(s) disclaim any responsibility for harm to persons or property resulting from the use of any ideas, methods, instructions, or products mentioned in the content.



© The Author(s) 2026. Open Access This article is licensed under a Creative Commons Attribution 4.0 International License (https://creativecommons.org/licenses/by/4.0/), which permits unrestricted use, sharing, adaptation, distribution and reproduction in any medium or format, for any purpose, even commercially, as long as you give appropriate credit to the original author(s) and the source, provide a link to the Creative Commons license, and indicate if changes were made.